CMS Physics Analysis Summary

Search for a third-generation leptoquark coupling to a τ lepton and a b quark through single, pair and nonresonant production at $\sqrt{s} = 13$ TeV

The CMS Collaboration

Abstract

A search is presented for a third-generation leptoquark (LQ) coupling to a τ lepton and a b quark. Events with τ leptons plus at least one jet originating from a b quark are considered, targeting the single and pair production of the LQ as well as nonresonant production via t-channel LQ exchange. The search is based on proton-proton collision data at a center-of-mass energy of $\sqrt{s} = 13$ TeV recorded with the CMS detector, corresponding to an integrated luminosity of 137 fb^{-1}. Upper limits are set on the LQ production cross section in the LQ mass range 0.5-2.3 TeV. Lower limits at 95% confidence level on the LQ mass are set in the 1.22-1.96 TeV range and for a coupling strength less than 2.5, depending on the LQ model. Upper limits are also set on the coupling strength of such LQs as a function of their mass. For a representative LQ mass of 2 TeV and a coupling strength of 2.5, an excess with a significance of 3.4 standard deviations above the standard model expectation is observed in the data. Consequently, the observed upper limits on the LQ production cross section are about three times larger than expected for this benchmark.

This document has been revised with respect to the version dated Jul 9, 2022.

1 Introduction

The standard model (SM) of particle physics is remarkably successful in describing matter and its fundamental interactions. In 2012, the discovery of a major missing piece, the Higgs boson was announced by the ATLAS and CMS experiments [1–3] at the CERN LHC. Despite its many successes, there are both theoretical and experimental reasons that imply the SM is not the final and most fundamental theory of nature.

Measurements of the $\overline{\mathrm{B}} \to \mathrm{D}\tau\overline{\nu}$ and $\overline{\mathrm{B}} \to \mathrm{D}^*\tau\overline{\nu}$ decay rates reported by the BaBar [4, 5], Belle [6–11], and LHCb [12–14] Collaborations collectively deviate from the SM predictions by about four standard deviations [15].

Leptoquark (LQ) models have recently received considerable theoretical interest as a possible explanation. These LQs are hypothetical color-triplet bosons, which carry both baryon and lepton quantum numbers and have fractional electric charge. They can either be scalar or vector bosons. They are predicted by many extensions of the SM, such as grand unification [16–23], and theories invoking technicolor [24–26] or compositeness [27]. An LQ that couples most strongly to third-generation fermions could offer consistent explanations [15, 28–53] for the $\overline{\mathrm{B}} \to \mathrm{D}\tau\overline{\nu}$, $\overline{\mathrm{B}} \to \mathrm{D}^*\tau\overline{\nu}$, and other B physics anomalies reported by LHCb [54–62] and Belle [63].

The production cross sections and decay widths of LQs in proton-proton (pp) collisions are determined by: the LQ mass m_{LQ}; its branching fraction β to a charged lepton and a quark; the coupling strength λ of the LQ-lepton-quark vertex; and the nonminimal coupling κ in case of vector LQs [64]. The LQs can be produced in pairs via gluon fusion or quark-antiquark annihilation, or singly via quark-gluon fusion. Recently, increasing attention has been given to the phenomenology of nonresonant production of two leptons with the LQ in the t channel as well, because this channel is more sensitive at high values of the coupling strength λ [65, 66]. Pair production of LQs is approximately independent of λ, while single and nonresonant production are dependent.

Currently, the most stringent limits on the production of an LQ decaying to a τ lepton and a bottom quark come from an analysis by the ATLAS Collaboration, in which a scalar (vector) LQ with mass below 1.25 (1.8) TeV was excluded in a search for LQ pair production [67]. A search for single production of the same decay mode was also performed by the CMS collaboration [68]. Other searches for LQs decaying to a top quark and a τ lepton or neutrino exploiting the full LHC 2016–2018 data set have been performed by CMS [69, 70] and ATLAS [67, 71].

This note presents a search that targets the single and pair production of scalar and vector LQs that decay exclusively to a τ lepton and a bottom quark, and a novel search for the nonresonant production of a τ lepton pair. Example Feynman diagrams of the signal processes at leading order (LO) are shown in Fig. 1. Single and pair production have a resonant final state that includes two τ leptons and at least one heavy-flavored jet. Nonresonant production will also have a final state with two τ leptons, and perhaps extra jets coming from gluon splitting or initial state radiation. The search is based on a data sample of pp collisions at a center-of-mass energy of 13 TeV recorded by the CMS experiment in 2016–2018, corresponding to an integrated luminosity of about 137 fb^{-1}. It exploits several decay channels of a τ lepton pair: fully hadronic ($\tau_{\mathrm{h}}\tau_{\mathrm{h}}$), semileptonic (e$\tau_{\mathrm{h}}$, $\mu\tau_{\mathrm{h}}$), and two fully leptonic channels (eμ, $\mu\mu$). Due to the large branching fraction, the semileptonic and fully hadronic channels are the most sensitive to an LQ signal with two τ leptons, while the events with two light leptons (eμ, $\mu\mu$) are used to constrain the SM backgrounds.
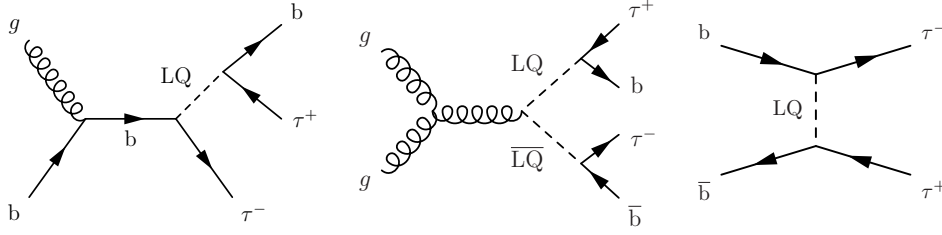
Figure 1: Dominant Feynman diagrams of the signal at LO: single (left) and pair LQ production (center), as well as nonresonant production of two τ leptons via t-channel LQ exchange (right).

2 The CMS detector

The central feature of the CMS apparatus is a superconducting solenoid of 6 m internal diameter, providing a magnetic field of 3.8 T. Within the solenoid volume, there are a silicon pixel and strip tracker, a lead tungstate crystal electromagnetic calorimeter (ECAL), and a brass and scintillator hadron calorimeter, each composed of a barrel and two endcap sections. Forward calorimeters extend the pseudorapidity coverage provided by the barrel and endcap detectors from $|\eta| < 3.0$ to $|\eta| < 5.2$. Muons are measured in gas-ionization detectors embedded in the steel flux-return yoke outside the solenoid.

Events of interest are selected using a two-tiered trigger system [72]. The first level, composed of custom hardware processors, uses information from the calorimeters and muon detectors to select events at a rate of around 100 kHz within a time interval of less than 4 μs. The second level, known as the high-level trigger, consists of a farm of processors running a version of the full event reconstruction software optimized for fast processing, and reduces the event rate to about 1 kHz before data storage.

A more detailed description of the CMS detector, together with a definition of the coordinate system used and the relevant kinematic variables, can be found in Ref. [73].

3 Simulated samples

3.1 Background samples

Samples of simulated events are used to devise selection criteria, and estimate and validate background predictions. The main sources of background are the pair production of top quarks ($t\bar{t}$), single top quark production, W and Z boson production in association with jets, denoted as "W + jets" and "Z + jets", diboson (WW, WZ, ZZ) production, and quantum chromodynamics (QCD) production of multijet events. The W + jets and Z + jets processes are simulated using the MADGRAPH5_aMC@NLO [74] generator (2.2.2 and 2.3.3) at LO precision with the MLM jet matching and merging scheme [75]. The same generator is also used for diboson production simulated at next-to-leading order (NLO) precision with the FxFx jet matching and merging scheme [76], whereas POWHEG [77–79] 2.0 and 1.0 are used for $t\bar{t}$ and single top quark production, respectively, at NLO precision [80–83]. The Z + jets, $t\bar{t}$, and single top processes are normalized using cross sections computed at next-to-next-to-leading order (NNLO) in perturbative QCD [84–86].

The event generators are interfaced with PYTHIA to model the parton showering and fragmentation, as well as the decay of the τ leptons. The PYTHIA parameters affecting the description of the underlying event are set to the CUETP8M1 (CP5) tune for all 2016 (2017 and 2018) samples [87, 88], except for the 2016 $t\bar{t}$ sample, for which CUETP8M2T4 [89] is used. The NNPDF3.0 parton distribution functions [90] (PDF) with the order matching that of the matrix element cal-

culations are used with all generators. Generated events are processed through a simulation of the CMS detector based on GEANT4 [91], and are reconstructed with the same algorithms used for data. The simulated samples include additional pp interactions per bunch crossing, referred to as "pileup". The effect of pileup is taken into account by generating concurrent collision events with PYTHIA. The simulated events are weighted such that the distribution of the number of pileup interactions matches that in data.

3.2 Signal samples

Signal samples are generated such that the LQ couples to b quark and τ lepton with a coupling strength λ. The total LQ decay width is smaller than experimental resolution for approximately $\lambda < 1.5$. The benchmark $\lambda = 1$ is used. Additional single LQ production samples with up to $\lambda = 2.5$ are included to take into account the increased width and larger number of soft events with invariant bτ mass much less than m_{LQ}.

A simplified $\tilde{R}_2$ model [34] was used to generate the signal samples with a scalar LQ. In the case of the vector LQ, a U_1 model [64] in which the LQ-fermion couplings in the Lagrangian are given by $\mathcal{L} \supset \lambda(\bar{b}_L \gamma^\mu \tau_L U_\mu + \bar{t}_L \gamma^\mu \nu_{\tau L} U_\mu) + \text{h.c.}$, with only left-handed fermions of the third generation. The signal samples are generated at LO precision using the MADGRAPH 2.6.1 [92] event generator with the five-flavor scheme (5FS), and NNPDF3.1 at LO is used as the PDF set. PYTHIA8 [93] is used for the parton showering, hadronization, and underlying event modelings. For the vector LQ, this analysis considers the scenario of nonminimal coupling $\kappa = 1$, which corresponds to the Yang-Mills case, and $\kappa = 0$, for the case of minimal coupling. The nonresonant production of two τ leptons via LQ t-channel exchange is generated assuming no interference with SM Drell-Yan processes, as the reduction of the signal yield in sensitive regions of the analysis is less than 5% for $\lambda > 1$ [66].

The cross sections of all signal processes are computed at LO with the models discussed above, except for the production of a scalar LQ pair, which is computed at NLO [94].

4 Event and object reconstruction

The reconstruction of observed and simulated events relies on the particle-flow (PF) algorithm [95], which combines information from the CMS subdetectors to reconstruct and identify the particles emerging from the pp collisions: charged and neutral hadrons, photons, muons, and electrons. This section describes how these PF objects are combined to reconstruct other physics objects such as jets, τ_h candidates, or missing transverse momentum (MET). The primary pp interaction vertex of an event is taken to be the reconstructed vertex corresponding to the hardest scattering in the event, evaluated using tracking information alone, as described in Section 9.4.1 of Ref. [96].

After being reconstructed by the PF algorithm, electrons are identified with a multivariate analysis (MVA) [97] discriminant that combines several quantities describing the track quality, the shape of the energy deposits in the ECAL, and the compatibility of the measurements from the tracker and the ECAL [98]. Selected electrons must pass a discriminant requirement that rejects electrons coming from photon conversions and are required to be isolated. The electron should have $p_T > 50\,\text{GeV}$, $|\eta| < 2.5$, and be within a longitudinal distance d_z of 0.2 cm and a radial distance d_{xy} of 0.045 cm with respect to the primary vertex.

Muons are identified with requirements on the quality of the track reconstruction and on the number of measurements in the tracker and the muon system [99], and are required to be isolated. Furthermore, the muon should have $p_T > 50\,\text{GeV}$, $|\eta| < 2.4$, and be within a longitudinal

distance $d_z < 0.2$ cm and a radial distance $d_{xy} < 0.045$ cm with respect to the primary vertex.

Jets are reconstructed from PF candidates using the anti-k_T clustering algorithm with a distance parameter of 0.4, implemented in the FASTJET library [100–102]. Charged PF candidates not associated with the primary vertex of the interaction are not considered when reconstructing jets. An offset correction is applied to jet energies to take into account the contribution from additional pp interactions within the same or nearby bunch crossings [103]. The energy of a jet is calibrated based on simulation and data through correction factors [103]. Further identification requirements are applied to distinguish genuine jets from those arising from pileup [104], and additional selection criteria on the energy fractions and multiplicity of charged and neutral particles are applied to each event to remove spurious jet-like features originating from isolated noise patterns in certain HCAL regions [105]. In this analysis, jets are required to have $p_T > 50$ GeV and $|\eta| < 4.7$, and must be separated from the selected leptons by $\Delta R = \sqrt{\Delta \eta^2 + \Delta \phi^2} > 0.5$.

Jets originating from the hadronization of bottom quarks are identified using the DeepCSV algorithm [106, 107]. DeepCSV is a deep neural network (DNN) with four hidden layers that is an extension of the combined secondary vertex (CSV) algorithm. It exploits observables related to the long lifetime and large mass of b hadrons. This analysis considers the loose working point (WP) of DeepCSV, which corresponds to a 10% misidentification rate for jets originating from light quarks or gluons. The efficiency of the loose WP in this analysis can reach up to 90%, depending on the jet p_T and η. Nevertheless, the efficiency degrades down to approximately 60% for $p_T > 500$ GeV.

The τ_h candidates are reconstructed with the hadron-plus-strips algorithm [108, 109], which is seeded with anti-k_T jets. This algorithm reconstructs τ_h candidates based on the number of charged hadrons and on the number of strips of ECAL crystals with energy deposits in the one-prong, one-prong-plus-π^0, three-prong and three-prong-plus-π^0 decay modes. A convolutional DNN-based discriminant is used to reduce the incidence of jets being misidentified as τ_h candidates, and makes use of isolation and lifetime information [109]. The medium WP of this discriminant is used in this analysis, with an efficiency of about 70% for a genuine τ_h, and about a 0.1% misidentification rate for quark and gluon jets. The same DNN training also provides discriminators to efficiently reject τ_h objects that have been mimicked by an electron or muon. Lastly, the τ_h candidate is required to have $p_T > 50$ GeV, $|\eta| < 2.3$, and be within a longitudinal distance d_z of 0.2 cm to the primary vertex.

The MET p_T^{miss} is magnitude of the vectorial sum of the $\vec{p}_T$ of all PF candidates [110, 111] originating from the primary vertex. It is adjusted for the effect of jet energy corrections.

5 Event selection

The present search considers the signature of events with high-p_T τ leptons with b quarks in the final state. This section discusses the event selection of this analysis to target that final state. First, Section 5.1 introduces a common preselection, which requires the events to be consistent with either the eτ_h, $\mu\tau_h$, $\tau_h\tau_h$, eμ, or $\mu\mu$ decay channel, where the electron, muon or τ_h object are assumed to be the visible products of τ lepton decay. Then event categories that target the resonant signal based on events with at least one high-p_T jet are defined in Section 5.2, and those targeting a nonresonant signal based on events with no high-p_T jets are defined in Section 5.3.

5.1 Common preselection

This analysis makes use of three type of triggers depending on the channel: triggers that were fired by single electrons for the $e\tau_h$ channel, by single muons for the $\mu\tau_h$, $e\mu$ and $\mu\mu$ channels, or by a pair of τ_h objects for the $\tau_h\tau_h$ channel. Some triggers are limited to $|\eta| < 2.1$, and if the event only passed such a trigger, the $|\eta|$ of the corresponding object is restricted to 2.1.

The $e\tau_h$ ($\mu\tau_h$) channel requires one electron (muon) and one τ_h candidate as described in Section 4. The selected lepton and τ_h should have an opening angle of $\Delta R > 0.5$ and have opposite-sign (OS) electric charges. If multiple combinations of such lepton and τ_h candidates are found, the pair formed by the candidates with the largest p_T is selected. In order to reject background events from $Z \to e^+e^-$ and $Z \to \mu^+\mu^-$, DNN-based anti-lepton discriminators are applied to the τ_h object in both channels. Therefore, in the $e\tau_h$ ($\mu\tau_h$) channel, a tight (very loose) WP of the anti-electron discriminator and a very loose (tight) WP of the anti-muon discriminator are applied.

Lastly, for both the $e\tau_h$ and $\mu\tau_h$ channels, "lepton vetoes" are applied, in order to reduce $Z + $ jets, $t\bar{t}$ production, and diboson backgrounds, as well as to keep orthogonality between the $e\tau_h$ and $\mu\tau_h$ channels: Events with additional isolated electrons or muons that pass looser identification criteria, and that do not match the previously selected τ decay candidates, are discarded.

Events in the $\tau_h\tau_h$ channel are required to have two τ_h candidates as detailed in Section 4. The τ_h pair should have an opening angle of $\Delta R > 0.5$ and have opposite-sign electric charges as well. As in the case of the semileptonic channels, antilepton discriminators and extra-lepton vetoes are applied. As there is little background from electrons or muons faking τ_h candidates, the loosest WPs are used.

As the single-muon triggers are used, the selection criteria of the muon candidate in the $e\mu$ and $\mu\mu$ channel follow exactly those of the $\mu\tau_h$ channel. The electron (muon) selection in $e\mu$ ($\mu\mu$) is also similar to that of the $e\tau_h$ ($\mu\tau_h$) channel.

5.2 Search for resonant LQ production

The final states of the single and pair process are characterized by two high-p_T τ leptons, and one or two high-p_T b quarks. In order to gain the best sensitivity to the LQ signal, the final discriminant, event categorization, and event selections have been optimized. The scalar sum of the p_T of the τ decay candidates (p_T^1, p_T^2), the leading jet (p_T^j), and p_T^{miss} is used as a discriminating variable,

$$S_T^{MET} \equiv p_T^1 + p_T^2 + p_T^j + p_T^{miss}. \tag{1}$$

Then two orthogonal event categories are constructed: the "0b" category, which requires zero loosely b-tagged jets with $p_T > 50\,\text{GeV}$, while the "$\geq$1b" category requires at least one such jet. An additional cut on the invariant mass of the visible τ-decay products of $m_{vis} > 100\,\text{GeV}$ is applied to remove Drell-Yan events, with negligible loss of signal.

5.3 Search for nonresonant LQ production

To increase the purity of the nonresonant signal, a low boost $|\eta_\ell + \eta_{\ell'}|/2 < 1.1$ and difference $\Delta\eta_{\ell\ell'} < 3$ between the two τ decay candidates are required. To make this category orthogonal to the categories described in Section 5.2, selected events are required to have no jets with $p_T > 50\,\text{GeV}$. This category will therefore be referred to as the "0j" category. After these
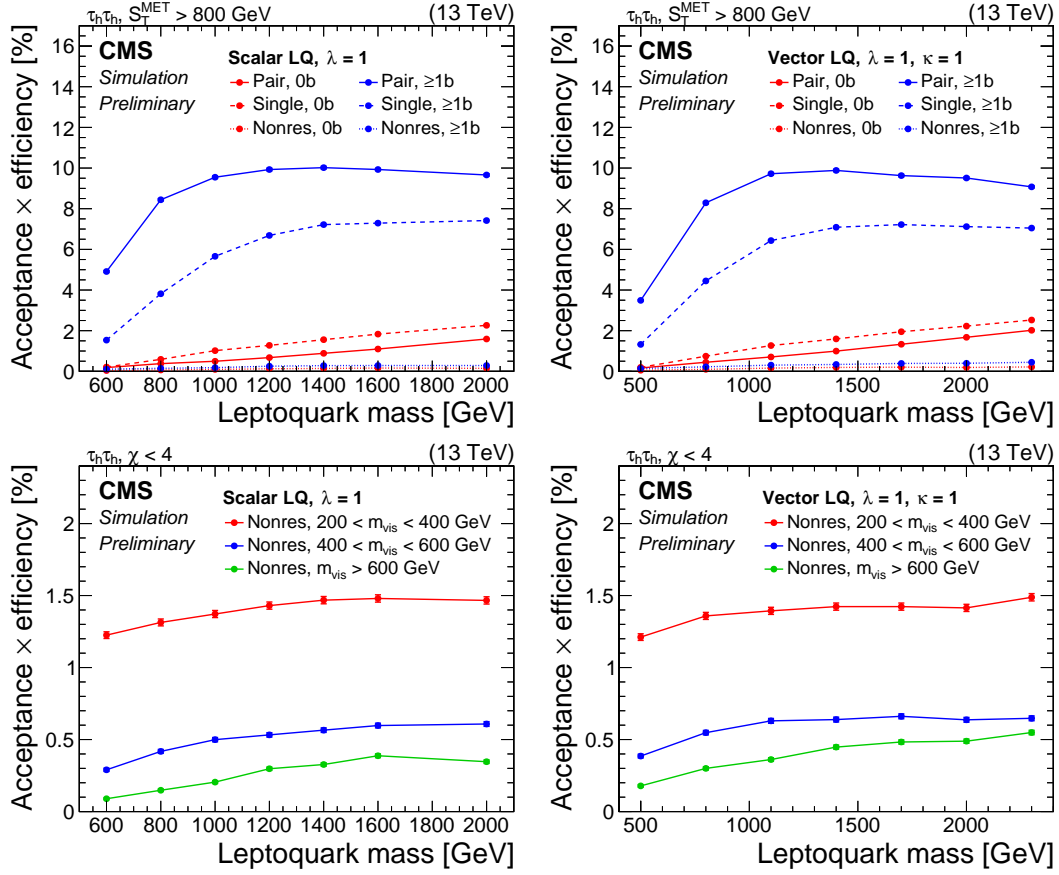
Figure 2: The product of acceptance and efficiency for a vector LQ signal in the $\tau_h\tau_h$ (left) and $\mu\tau_h$ (right) channels of the 0b and $\geq$1b (top), and the 0j categories (bottom) are shown. Vertical bars indicate the statistical uncertainty in the efficiency.

selections, the events are separated into three bins of the visible mass m_{vis}: 200–400 GeV, 400–600 GeV and larger than 600 GeV, because the signal purity increases with m_{vis}.

This analysis looks for the angular separation between two taus, defined as, $\chi = \exp(2y^\star)$ where $y^\star = \frac{1}{2}|y_1 - y_2|$, while y_1 and y_2 are the rapidities of the two leading jets, and p_z is the projection of the jet momentum onto the beam axis. The choice of this variable is motivated by the fact that the χ distribution in Rutherford scattering is flat. It also allows to examine more easily signatures of new physics that might have a more isotropic angular distribution than the QCD multijet background, appearing as an excess at low values of χ. The χ distribution is then measured over the range $1 < \chi < 30$, which implies a maximum value of $y^* = 1.7$.

The product of acceptance and efficiency for the vector LQ signal in the various signal categories is shown in Fig. 2 as a function of m_{LQ}. The scalar LQ signal has a very similar efficiency in all cases. The efficiencies are restricted to the sensitive region of the respective final discriminants. In the $\tau_h\tau_h$ channel of the $\geq$1b category, the selection efficiency for the LQ pair production events varies with mass between approximately 3.5 and 10%, while the efficiency for the single production varies between 1.0 and 7.5%. The efficiency for resonant production in $\geq$1b is smaller at lower m_{LQ} due to a softer p_T spectrum.

6 Background estimation

For the search of a resonant LQ signal in the $\geq 1b$ category, the dominant background in all search channels stems from $t\bar{t}$ production because of the presence of genuine electrons, muons, τ leptons, and b quark jets from top decays. For the nonresonant search in the 0j category on the other hand, the main background in the sensitive region is Drell-Yan production.

6.1 Background estimation for the $\ell\tau_\mathrm{h}$ & $\tau_\mathrm{h}\tau_\mathrm{h}$ channels

For the $e\tau_\mathrm{h}$, $\mu\tau_\mathrm{h}$ and $\tau_\mathrm{h}\tau_\mathrm{h}$ channels all SM background processes, except for the QCD multijet and $W+$jets backgrounds, are estimated using simulation.

The background arising from jets misidentified as τ_h candidates, denoted as "$j \to \tau_\mathrm{h}$ fakes", is estimated in a data-driven way from control regions (CRs) in data, using the so-called fake-factor (FF) method. The method was fully implemented and cross-checked for the 2016 dataset in Ref. [112, 113], which has similar event selection and final states to the present analysis. These backgrounds consist dominantly of QCD multijet and $W+$jets events. To avoid over-counting, simulated events that contain a selected τ_h object that does not originate from a lepton or genuine τ lepton at generator-level are discarded. The $j \to \tau_\mathrm{h}$ fake component of each simulated background is omitted to avoid overcounting.

The FF method defines an application region (AR) containing the same selection criteria as in the signal region (SR), except for an inverted τ_h isolation requirement for one of the two τ_h candidates. The AR is primarily populated by events with jets misidentified as τ_h candidates, and has contamination from genuine hadronic τ decays at the level of a few percent or below. The ratio of the number of events with a misidentified τ_h in the AR to the number in the SR, i.e., the FF, is assumed to be the same as the ratio measured in samples with a same-sign (SS) pair. The FF is then applied to the number of events in the AR to estimate the number of events with a misidentified τ_h in the SR. The FF is calculated as a function of the p_T and decay mode of the τ_h candidate, and it ranges from 0.1 to 0.25. Since the presence of small backgrounds in the AR that contain a genuine τ_h results in up to a 2% underestimation of the number of events with a misidentified τ_h in the SR, a correction is applied based on the fractions of these processes in simulated events. Corresponding uncertainties are incorporated in the fit model, as described in Section 7. The FF method for the $\tau_\mathrm{h}\tau_\mathrm{h}$ channel is similar, with the exception that a weight factor of 0.5 is applied to take combinatorial effects into account.

The FF method is tested in two validation regions (VRs); one is constructed by inverting the leading jet p_T requirement (i.e., $p_\mathrm{T} < 50\,\mathrm{GeV}$) and the other by using events with two τ_h candidates that do not fulfill the tight isolation criteria used to define the SR. For both VRs, all other selection criteria are kept identical to the SR, except that the b tagging requirement is removed to increase the number of events. The signal contamination is negligible in both VRs. Agreement between data and simulation is found, within statistical uncertainties, demonstrating the validity of the fake-factor method.

6.2 Background estimation for the $e\mu$ & $\mu\mu$ channels

In the $e\mu$ and $\mu\mu$ channels all SM background processes, except for the QCD multijet, are estimated using simulation, and are normalized according to the theoretical cross section.

The QCD multijet background is small and is estimated from a SS control region. In this control region, the QCD multijet shape is constructed by subtracting from observed data the simulated SM backgrounds in each histogram bin. This shape is rescaled by an extrapolation factor to obtain the expected QCD multijet background in the OS signal region. It is measured in a high-

purity QCD multijet sample by inverting the lepton isolation requirement, and is found to be approximately 2.4.

7 Systematic uncertainties

7.1 Normalization uncertainties

The uncertainty in the integrated luminosity varies between 1.2 and 2.5%, depending on the year [114–116] and affects the normalization of the signal and background processes that are based on simulation. Uncertainties in the electron or muon identification and trigger efficiency amount to 2% each [117]. The τ_h trigger efficiency has been measured using the "tag-and-probe" technique [108] and an overall rate uncertainty of 10% is assigned. For events where electrons or muons are misidentified as τ_h candidates, predominantly $Z \to e^+e^-$ events in the $e\tau_h$ channel and $Z \to \mu^+\mu^-$ events in the $\mu\tau_h$ channel, rate uncertainties of 12 and 25% [118], respectively, are applied, as determined by a tag-and-probe method.

The QCD multijet background estimation in $e\mu$ and $\mu\mu$ is found to have rate uncertainties up to 20%. The uncertainty in the Z + jets cross-section is estimated using a dedicated CR in events with two τ_h candidates and at least one b-tagged jet. A 30% uncertainty is assigned to the Z + jets cross section in the $\geq 1b$ category on the basis of the expected fluctuations in the total number of data events in this CR. In the other signal categories, the uncertainty in the NNLO computation is given as 3%. The uncertainties in the cross section for the $t\bar{t}$, diboson and single top quark processes are 5.5, 6 and 5.5%, respectively. These uncertainties in the cross sections are treated as correlated between the years, but uncorrelated between 0j and the other signal categories.

7.2 Shape uncertainties

The τ_h identification efficiency scale factors (SFs) are applied as a function of p_T for the semileptonic channels ($\mu\tau_h$ and $e\tau_h$) and are decay mode dependent for the $\tau_h\tau_h$ channel. The uncertainty in the τ_h identification efficiency is taken as the total uncertainty in the measurement, and is fully uncorrelated between the years.

The uncertainty in the τ_h energy scale depends on the τ_h decay mode and p_T, and varies between 0.6 and 1.4% for $p_T < 34$ GeV, and between 1 and 4% for $p_T > 170$ GeV, with a simple linear interpolation between the respective uncertainties for 34 GeV $< p_T < 170$ GeV. It is only applied to the background components with genuine τ_h, namely those in simulated Z + jets, $t\bar{t}$ and LQ events. It is uncorrelated between the years and signal categories, but correlated between the different channels. Similarly, for events where a muon or electron is misidentified as a τ_h candidate, a shape uncertainty is derived by varying the τ_h energy scale by 3%.

The uncertainties in the jet energy scale are up to 4%, depending on the jet p_T and η [103]. The uncertainties in the jet energy scale and resolution are taken into account as shape uncertainties by simply taking the one-standard deviation variations of the corrections, and propagating them to all the affected variables in the analysis (including jet p_T, jet multiplicity, b tag multiplicity, p_T^{miss} and S_T^{MET}). They are uncorrelated between the years, but correlated between the different decay channels of each signal category.

The uncertainties in b tagging efficiency of heavy flavors (b and c quark) and misidentification rate of light flavors (u, d or s quark, or gluon) are taken into account from the uncertainties in the b tagging SFs. The uncertainty in the heavy flavor efficiencies is kept correlated between b and c quarks, and similarly between the uncertainty in the misidentification rate of light

Table 1: The sources of uncertainty considered, categorized as to whether they affect the normalization or shape of the distributions. "s.d." refers to the standard deviation of the input variable.

Systematic source	Channel				
	$e\tau_h$	$\mu\tau_h$	$\tau_h\tau_h$	$e\mu$	$\mu\mu$
Normalization					
Integrated luminosity			1.2–2.5%		
Electron ident.	2%	—	—	2%	—
Electron trigger	2%	—	—	—	—
Muon ident.	—	2%	—	2%	2%
Muon trigger	—	2%	—	2%	2%
τ_h trigger	—	—	10%	—	—
e misident. as τ_h rate	12%	—	12%	—	—
μ misident. as τ_h rate	—	25%	25%	—	—
p_T^{miss} scale			Up to 4%		
QCD multijet normalization	—	—	—	20%	20%
Z + jets cross section		20% in $\geq$1b, 3% otherwise			
$t\bar{t}$ cross section			5.5%		
W + jets cross section	—	—	—	6%	6%
Diboson cross section			6%		
Single top quark cross section			5.5%		
FF norm., 0b	3.0%	2.5%	2.2%	—	—
FF norm., $\geq$1b	2.5%	1.8%	1.7%	—	—
FF norm., 0j, $200 < m_{\mathrm{vis}} < 400\,\mathrm{GeV}$	1.4%	1.1%	0.3%	—	—
FF norm., 0j, $400 < m_{\mathrm{vis}} < 600\,\mathrm{GeV}$	3.9%	3.1%	3.0%	—	—
FF norm., 0j, $m_{\mathrm{vis}} > 600\,\mathrm{GeV}$	4.0%	3.6%	3.0%	—	—
Jet energy scale			5% in 0j		
Shape					
τ_h ident. efficiency		$\pm$1 s.d. in SF		—	—
τ_h energy scale		$\pm$1 s.d. on the energy scale		—	—
μ misident. as τ_h energy scale		$\pm$1% on the energy scale		—	—
e misident. as τ_h energy scale		$\pm$1 s.d. on the energy scale		—	—
FF shape variations		Syst. shape variations		—	—
b tagging efficiency		$\pm$1 s.d. in b tagging SFs			
b tagging mistag rate		$\pm$1 s.d. in b tagging SFs			
Jet energy scale		$\pm$1 s.d. in SF in 0b, $\geq$1b			
Jet energy resolution		$\pm$1 s.d. in SF in 0b, $\geq$1b			
PDF variations		Envelope of PDF variations			
μ_R & μ_F variations		Envelope of scale variations			
Z p_T reweighting		Weight applied $\pm$50%			
Top p_T reweighting		(top p_T weight)^p with $p = 5$ or -5			

flavors. Most of the shape variations have little dependence on $S_\mathrm{T}^\mathrm{MET}$, with about a 1% change in overall yield in the $\geq 1b$ category, and less than 3% in 0b. The uncertainties are only partially correlated between the years.

The uncertainties of the FF method include the total systematic uncertainties in the measurement of the FFs in each of the $W +$ jets, $t\bar{t}$ and QCD CRs, as well as the statistical uncertainty in the fit of the FFs. The latter uncertainty is split into the 0 and $\geq 1j$ bins of the FF parametrization. They are treated as uncorrelated between the years and signal categories, as the dominant background process can differ. The shape uncertainties are normalized to the nominal $j \to \tau_\mathrm{h}$ event yield, and their total variation in event yield is taken as one normalization nuisance parameter, which is summarized in Table 1. Each of these uncertainties is applied to the $j \to \tau_\mathrm{h}$ background estimation obtained by the FF method.

The uncertainty in the Z p_T reweighing is applied by varying the weight up and down by 50%. The top p_T reweighting is not applied nominally, shape variation is created by applying the top p_T reweighting five times, so it can be well constrained by the eμ region.

The shape uncertainties in the renormalization and factorization scales μ_R and μ_F are computed by taking the envelope of all variations, varying each scale simultaneously by the same or different factor (0.5, 1 or 2) while keeping the total yield constant. Extreme combinations $(\mu_\mathrm{R}, \mu_\mathrm{F}) = (0.5, 2)$ or $(2, 0.5)$ are excluded. Similarly, the shape uncertainties due to the PDFs are taken into account by creating a symmetric envelope [119].

Finally, uncertainties related to the limited number of simulated events are taken into account with the Barlow-Beeston-lite approach [120, 121]. They are considered for all bins of the distributions that are used to extract the results. They are kept uncorrelated across the different samples and across the bins of a single distribution.

All systematic uncertainties are summarized in Table 1.

8 Results

A binned maximum likelihood fit [122] of the observed $S_\mathrm{T}^\mathrm{MET}$ and χ distributions in all channels, event categories and data-taking periods is used to search for a possible signal over the expected background. For maximal sensitivity and exclusion power, the three production modes considered in this analysis are treated as one signal. Therefore, this analysis derives an upper limit on the sum of their cross sections, $\sigma^\mathrm{tot} \equiv \sigma^\mathrm{single} + \sigma^\mathrm{pair} + \sigma^\mathrm{nonres}$.

Figure 3 shows exemplary postfit distributions of $S_\mathrm{T}^\mathrm{MET}$ in the $\tau_\mathrm{h}\tau_\mathrm{h}$ and eμ channels in the 0b category and $\geq 1b$ categories, while Fig. 4 shows the postfit distributions of χ in the $400\,\mathrm{GeV} < m_\mathrm{vis} < 600\,\mathrm{GeV}$ and $m_\mathrm{vis} > 600\,\mathrm{GeV}$ bins of the 0j category. They are obtained after adding up per data-taking period the distributions of the same channel and category. The $S_\mathrm{T}^\mathrm{MET}$ distributions include the overflow in the last bin. The uncertainty bands include the statistical uncertainties and all postfit uncertainties on the expectation. The total LQ signal for the benchmark $M = 2000\,\mathrm{GeV}$ with $\lambda = 2.5$ and $\kappa = 1$ is overlaid. They are normalized to the fitted cross section. The binning of all histograms is adjusted such that the total statistical uncertainty in the SM background expectation of a given bin does not exceed 20%.

Table 2 shows the best-fit signal cross section with the corresponding significance for different LQ production modes. For lower masses and coupling strengths λ, the observed data agree with the standard model expectation within one standard deviation. At higher masses and coupling strengths, however, an excess with a significance of up to 3.4 standard deviations
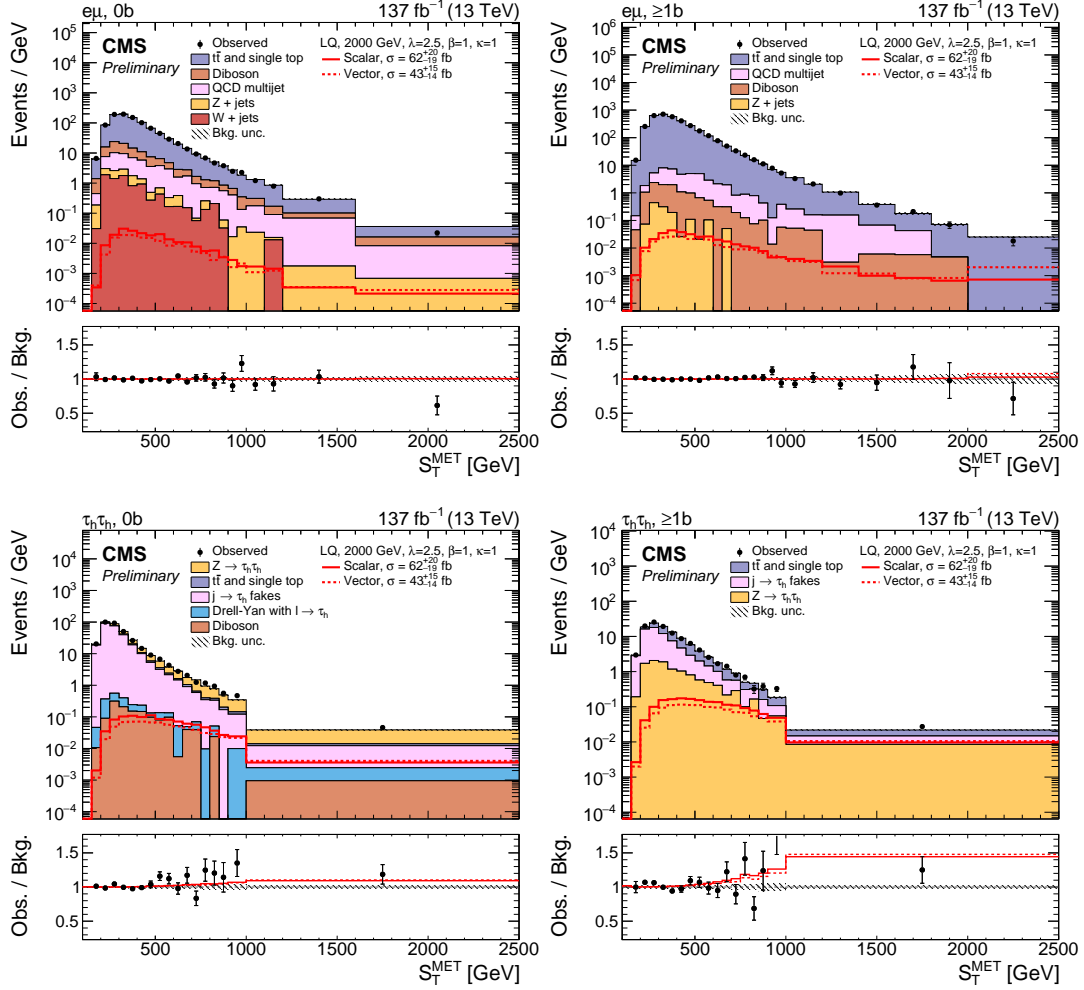
Figure 3: Postfit distributions of S_T^{MET} for the combined 2016–2018 dataset after a simultaneous fit of the scalar LQ signal to the data in each data-taking period. The last bin includes the overflow. The eμ (top) and $\tau_h\tau_h$ (bottom) channels in the 0b (left) and $\geq$1b (right) category are shown. The fitted signal distributions for the total scalar (solid red) and vector LQ model (dashed red) with a mass of 2000 GeV and a coupling strength of $\lambda = 2.5$ are overlaid to illustrate the sensitivity. They include the single and pair LQ production, as well as the nonresonant production of a τ lepton pair. The lower panel shows the ratio between the observed data and background from the S+B fit (black). The hatched uncertainty bands include the total postfit uncertainties in the background.
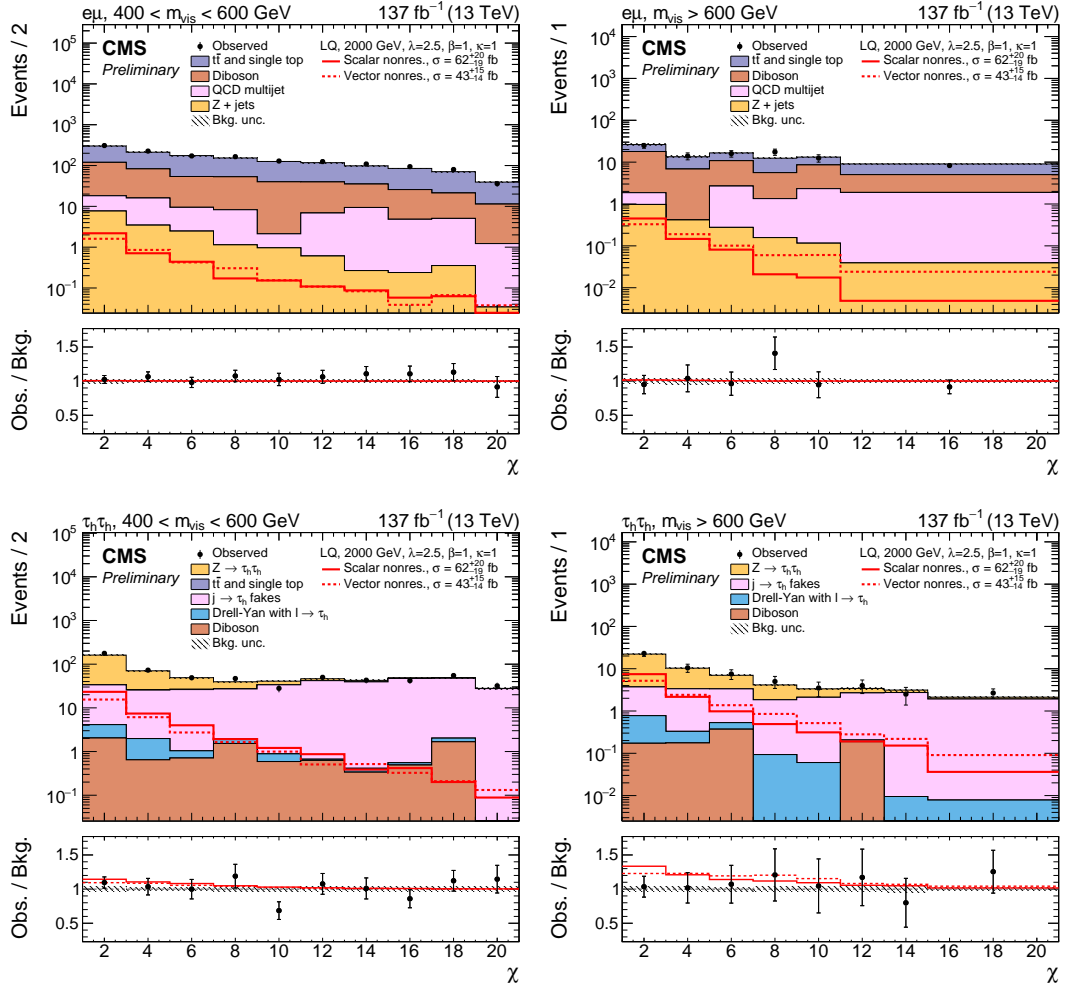
Figure 4: Postfit distributions of χ for the combined 2016–2018 dataset after a simultaneous fit of the scalar LQ signal to the data in each data-taking period. The eμ (top) and $\tau_h\tau_h$ (bottom) channels in the $400\,\text{GeV} < m_{\text{vis}} < 600\,\text{GeV}$ (left) and $m_{\text{vis}} > 600\,\text{GeV}$ (right) category are shown. The fitted nonresonant signal for the scalar (solid red) and vector LQ model (dashed red) with a mass of $2000\,\text{GeV}$ and a coupling strength of $\lambda = 2.5$ are overlaid to illustrate the sensitivity. The lower panel shows the ratio between the observed data and background from the S+B fit (black). The hatched uncertainty bands include the total postfit uncertainties in the background.

Table 2: Best-fit LQ cross sections σ for various masses and coupling strengths λ, and the corresponding significance z (given in standard deviations) for different production modes individually, as well as their combination.

Signal	$m_{\mathrm{LQ}} = 1400\,\mathrm{GeV}$		$m_{\mathrm{LQ}} = 2000\,\mathrm{GeV}$	
	σ [pb]	z	σ [fb]	z
Scalar				
Pair	$0.24^{+0.47}_{-0.45}$	0.5	$0.22^{+0.41}_{-0.39}$	0.0
Single, $\lambda = 1$	$1.15^{+0.95}_{-0.92}$	1.3	$0.64^{+0.68}_{-0.65}$	1.0
Single, $\lambda = 2.5$	$9.1^{+5.6}_{-5.3}$	1.7	18^{+11}_{-11}	1.7
Nonres.	70^{+23}_{-22}	3.4	63^{+20}_{-19}	3.5
Total, $\lambda = 1$	$1.7^{+1.9}_{-1.8}$	0.9	$9.6^{+6.2}_{-5.9}$	1.7
Total, $\lambda = 2.5$	43^{+16}_{-15}	2.9	62^{+20}_{-19}	3.4
Vector, $\kappa = 0$				
Pair	$0.24^{+0.46}_{-0.44}$	0.0	$0.24^{+0.41}_{-0.39}$	0.0
Single, $\lambda = 1$	$1.00^{+0.89}_{-0.85}$	1.2	$0.60^{+0.66}_{-0.63}$	1.0
Single, $\lambda = 2.5$	$9.1^{+6.5}_{-6.2}$	1.5	25^{+18}_{-17}	1.4
Nonres.	58^{+18}_{-17}	3.5	51^{+16}_{-15}	3.5
Total, $\lambda = 1$	$1.2^{+1.5}_{-1.4}$	0.8	$7.7^{+5.1}_{-4.8}$	1.7
Total, $\lambda = 2.5$	$12.2^{+7.1}_{-6.8}$	1.8	43^{+15}_{-14}	3.1
Vector, $\kappa = 1$				
Pair	$0.24^{+0.46}_{-0.44}$	0.0	$0.24^{+0.41}_{-0.39}$	0.0
Single, $\lambda = 1$	$1.00^{+0.89}_{-0.85}$	1.2	$0.60^{+0.66}_{-0.63}$	1.0
Single, $\lambda = 2.5$	$9.1^{+6.5}_{-6.2}$	1.5	25^{+18}_{-17}	1.4
Nonres.	58^{+18}_{-17}	3.5	51^{+16}_{-15}	3.5
Total, $\lambda = 1$	$0.42^{+0.69}_{-0.66}$	0.0	$1.3^{+1.5}_{-1.4}$	0.5
Total, $\lambda = 2.5$	$12.2^{+7.1}_{-6.8}$	1.8	43^{+15}_{-14}	3.1

above the SM background expectation is found. This excess is observed across several channels, as well as in both the χ and $S_{\mathrm{T}}^{\mathrm{MET}}$ distributions in the different event categories. The excess is most prominent for the nonresonant signal in the analysis, which contributes to the combined excess increasingly as larger LQ masses and couplings are considered. The significance of the nonresonant signal by itself has no strong dependence on m_{LQ} or λ, but when combined with the pair and single production contributions to the total LQ signal, the excess at lower LQ masses and couplings is reduced.

Figure 5 shows a histogram the number of events of χ and $S_{\mathrm{T}}^{\mathrm{MET}}$ bins reordered and stacked by $S/(S+B)$, where S (B) is the total fitted signal (background) yield in a given bin. A vector LQ model with $m_{\mathrm{LQ}} = 1400(2000)\,\mathrm{GeV}$ and $\lambda = 1(2.5)$ is assumed. The excess becomes more evident at high λ, where more bins from the 0j category appear at high $S/(S+B)$ due to increased sensitivity to a nonresonant signal.

We set an expected upper limit on the cross section of single, pair and nonresonant production, as well as their sum, with the asymptotic $\mathrm{CL_s}$ modified-frequentist criterion [122–125]. The single production cross section roughly scales with λ^2 at lower values of $\lambda < 1.5$, while the nonresonant production cross section is proportional to λ^4. Consequently, an upper limit on

the total cross section σ^{tot} can be derived for different values of λ. To exclude regions of the λ-m_{LQ} phase space, the upper limit on λ at 95% CL is computed by varying λ.

The observed and expected upper limits on the total cross section of scalar and vector LQ production with $\lambda = 1$ at 95% CL are shown in Figs. 6 and 7, respectively.

Figures 8 and 9 show the upper limit on λ at 95% CL as a function of m_{LQ} for the scalar and vector model. They include one line for each production mode, as well as their combination, which allows for the exclusion of a larger region at higher values of λ, where the single and nonresonant production start to contribute more significantly. The region with blue shading shows the parameter space preferred by one of the models proposed to explain the B physics lepton anomalies. At 95% confidence level, LQ masses below 1.25 TeV are excluded for the scalar model with $\lambda = 1$, and below 1.53 (1.86) GeV for the vector model with $\lambda = 1$ and non-minimal coupling $\kappa = 0(1)$. At $\lambda = 2.5$, the lower limits are 1.37 TeV for a scalar model, and 1.86 (1.96) GeV for a vector model with $\kappa = 0(1)$.

9 Summary

This note has reported a search for a third-generation leptoquark (LQ) decaying to a τ lepton and a b quark. Events with τ leptons and one jet originating from a b quark were considered, targeting the single and pair production of the LQ, as well as the nonresonant production with the LQ in the t channel. The search used proton-proton collision data at a center-of-mass energy of 13 TeV recorded with the CMS detector corresponding to an integrated luminosity of 137 fb^{-1}. Upper limits have been set on the third-generation scalar LQ production cross section as a function of the LQ mass, and results were compared with theoretical predictions to obtain lower limits on the LQ mass. At 95% confidence level, third-generation LQ decaying to a τ lepton and a b quark with unit coupling are excluded for masses below 1.25 TeV for a scalar model, and below 1.53 (1.86) GeV for a vector model with non-minimal coupling $\kappa = 0(1)$, while at $\lambda = 2.5$ the lower limits are 1.37 TeV for a scalar model, and 1.86 (1.96) GeV for a vector model with $\kappa = 0(1)$. Upper limits are also set on the coupling strength of such LQs as a function of their mass.

The observed data agree with the standard model expectation within 2 standard deviations below a coupling strength of $\lambda = 1.5$. For a representative LQ mass of 2 TeV and a coupling strength of 2.5, an excess with a significance of 3.4 standard deviations above the standard model expectation is observed in the data. Consequently, the observed upper limits on the LQ production cross section are about three times larger than expected for this benchmark.
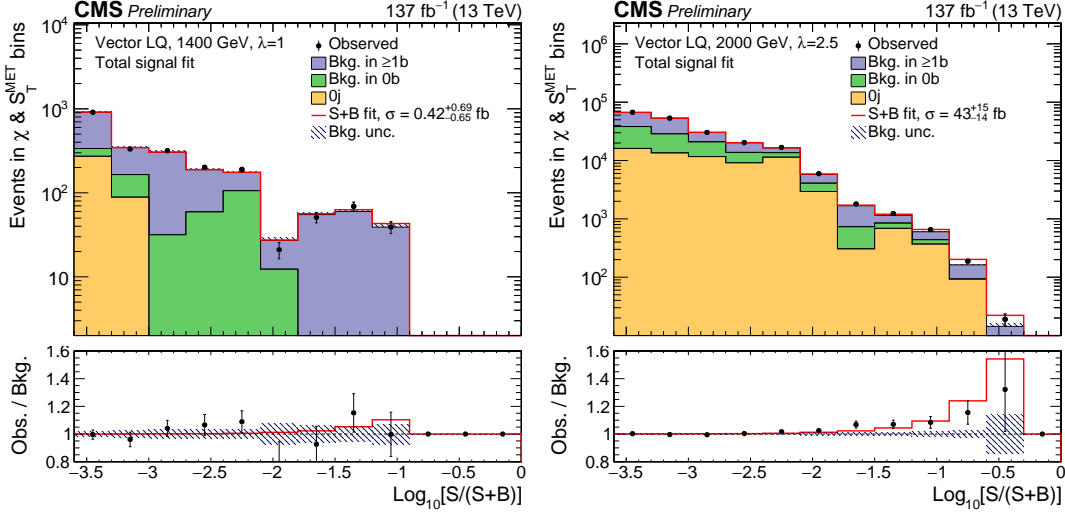
Figure 5: Histograms of $\log_{10}\left[S/(S+B)\right]$ counting events in all bins, assuming a vector LQ with $m_{\text{LQ}} = 1400\,\text{GeV}$ and $\lambda = 1.0$ (left), or $m_{\text{LQ}} = 2000\,\text{GeV}$ and $\lambda = 2.5$ (right). The $\log_{10}\left[S/(S+B)\right]$ is computed per bin of the postfit χ and $S_{\text{T}}^{\text{MET}}$ distributions, using an S+B fit model. The total LQ signal strength (single, pair & nonresonant) is fitted simultaneously. The lower panel shows the ratio of the observed data to the expected background from the S+B fit. The expected background is grouped by jet categories in stacked histograms.
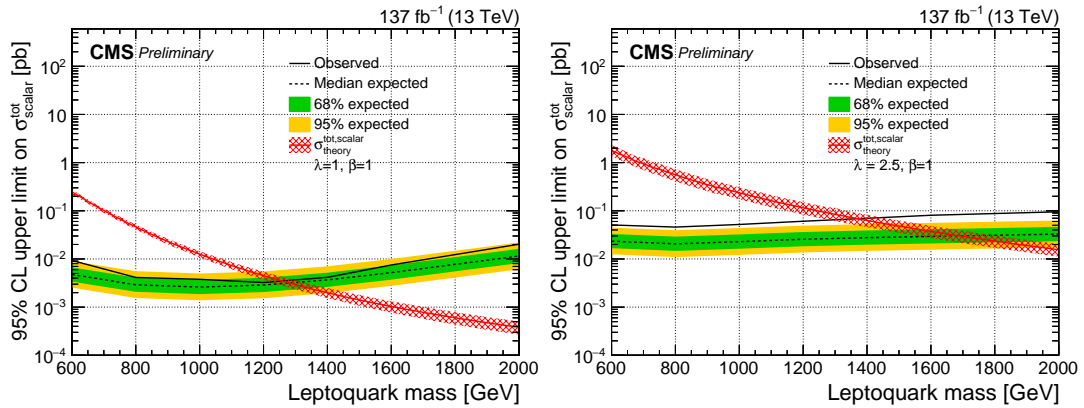

Figure 6: The observed and expected upper limit on the total cross section of a scalar LQ signal with $\lambda = 1$ (left) and 2.5 (right) at 95% CL. The inner (green) band and the outer (yellow) band indicate the regions containing 68 and 95%, respectively, of the distribution of limits expected under the background-only hypothesis.
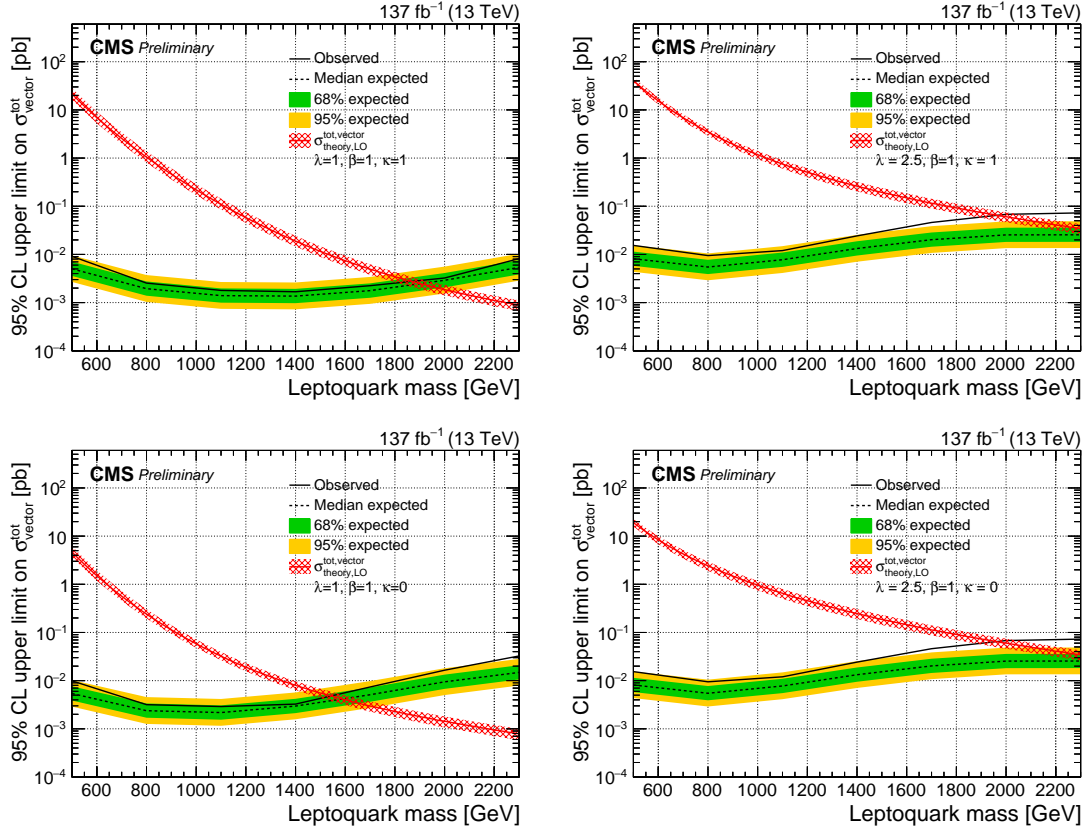
Figure 7: The observed and expected upper limit on the total cross section of a vector LQ signal with $\lambda = 1$ (left) and 2.5 (right) at 95% CL. The top (bottom) row assumes a nonminimal coupling of $\kappa = 1$ (0). The inner (green) band and the outer (yellow) band indicate the regions containing 68 and 95%, respectively, of the distribution of limits expected under the background-only hypothesis.
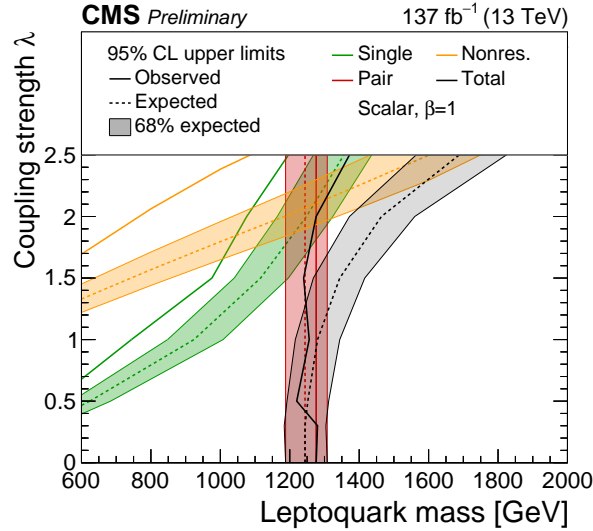

Figure 8: The observed and expected upper limit at 95% CL on the coupling strength λ of a scalar LQ. All years and all channels in each category are combined. The limits derived for the single (green), pair (red), nonresonant (orange) and total LQ production (black) are shown. The hatched bands around the expected limit lines correspond to the regions containing 68% of the distribution of limits expected under the background-only hypothesis.
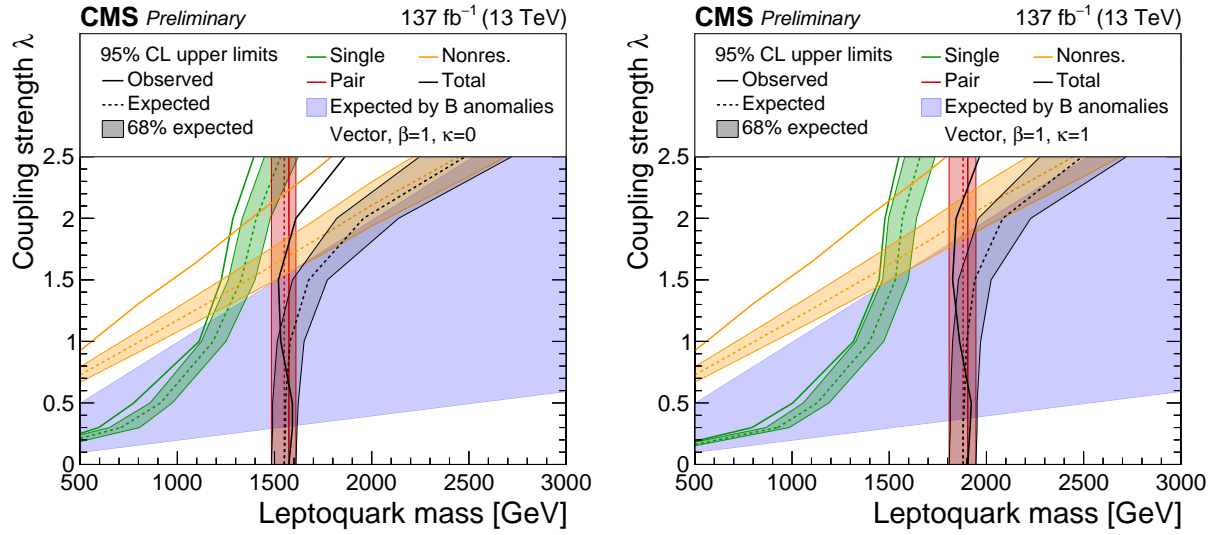
Figure 9: The observed and expected upper limit at 95% CL on the coupling strength λ of a vector LQ model with $\kappa = 0$ (left) and $\kappa = 1$ (right). All years and all channels in each category are combined. The limits derived for the single (green), pair (red), nonresonant (orange) and total LQ production (black) are shown. The hatched bands around the expected limit lines correspond to the regions containing 68% of the distribution of limits expected under the background-only hypothesis. The region with blue shading shows the parameter space preferred by one of the models proposed to explain anomalies observed in B physics.

References

[1] CMS Collaboration, "Observation of a new boson at a mass of 125 GeV with the CMS experiment at the LHC", *Phys. Lett. B* **716** (2012) 30, `doi:10.1016/j.physletb.2012.08.021`, `arXiv:1207.7235`.

[2] ATLAS Collaboration, "Observation of a new particle in the search for the Standard Model Higgs boson with the ATLAS detector at the LHC", *Phys. Lett. B* **716** (2012) 1, `doi:10.1016/j.physletb.2012.08.020`, `arXiv:1207.7214`.

[3] CMS Collaboration, "Observation of a new boson with mass near 125 GeV in pp collisions at $\sqrt{s}$ = 7 and 8 TeV", *JHEP* **06** (2013) 081, `doi:10.1007/JHEP06(2013)081`, `arXiv:1303.4571`.

[4] BaBar Collaboration, "Evidence for an excess of $\bar{B} \to D^{(*)}\tau^-\bar{\nu}_\tau$ decays", *Phys. Rev. Lett.* **109** (2012) 101802, `doi:10.1103/PhysRevLett.109.101802`, `arXiv:1205.5442`.

[5] BaBar Collaboration, "Measurement of an excess of $\bar{B} \to D^{(*)}\tau^-\bar{\nu}_\tau$ decays and implications for charged Higgs bosons", *Phys. Rev. D* **88** (2013) 072012, `doi:10.1103/PhysRevD.88.072012`, `arXiv:1303.0571`.

[6] Belle Collaboration, "Observation of $B^0 \to D^{*-}\tau^+\nu_\tau$ decay at Belle", *Phys. Rev. Lett.* **99** (2007) 191807, `doi:10.1103/PhysRevLett.99.191807`, `arXiv:0706.4429`.

[7] Belle Collaboration, "Observation of $B^+ \to \bar{D}^{*0}\tau^+\nu_\tau$ and evidence for $B^+ \to \bar{D}^0\tau^+\nu_\tau$ at Belle", *Phys. Rev. D* **82** (2010) 072005, `doi:10.1103/PhysRevD.82.072005`, `arXiv:1005.2302`.

[8] Belle Collaboration, "Measurement of the branching ratio of $\bar{B} \to D^{(*)}\tau^-\bar{\nu}_\tau$ relative to $\bar{B} \to D^{(*)}\ell^-\bar{\nu}_\ell$ decays with hadronic tagging at Belle", *Phys. Rev. D* **92** (2015) 072014, `doi:10.1103/PhysRevD.92.072014`, `arXiv:1507.03233`.

[9] Belle Collaboration, "Measurement of the branching ratio of $\bar{B}^0 \to D^{*+}\tau^-\bar{\nu}_\tau$ relative to $\bar{B}^0 \to D^{*+}\ell^-\bar{\nu}_\ell$ decays with a semileptonic tagging method", *Phys. Rev. D* **94** (2016) 072007, `doi:10.1103/PhysRevD.94.072007`, `arXiv:1607.07923`.

[10] Belle Collaboration, "Measurement of the τ lepton polarization and $R(D^*)$ in the decay $\bar{B} \to D^*\tau^-\bar{\nu}_\tau$", *Phys. Rev. Lett.* **118** (2017) 211801, `doi:10.1103/PhysRevLett.118.211801`, `arXiv:1612.00529`.

[11] Belle Collaboration, "Measurement of the τ lepton polarization and $R(D^*)$ in the decay $\bar{B} \to D^*\tau^-\bar{\nu}_\tau$ with one-prong hadronic τ decays at Belle", *Phys. Rev. D* **97** (2018) 012004, `doi:10.1103/PhysRevD.97.012004`, `arXiv:1709.00129`.

[12] LHCb Collaboration, "Measurement of the ratio of branching fractions $\mathcal{B}(\bar{B}^0 \to D^{*+}\tau^-\bar{\nu}_\tau)/\mathcal{B}(\bar{B}^0 \to D^{*+}\mu^-\bar{\nu}_\mu)$", *Phys. Rev. Lett.* **115** (2015) 111803, `doi:10.1103/PhysRevLett.115.159901`, `arXiv:1506.08614`. [Erratum: `doi:10.1103/PhysRevLett.115.111803`].

[13] LHCb Collaboration, "Measurement of the ratio of the $B^0 \to D^{*-}\tau^+\nu_\tau$ and $B^0 \to D^{*-}\mu^+\nu_\mu$ branching fractions using three-prong τ-lepton decays", *Phys. Rev. Lett.* **120** (2018), no. 17, 171802, `doi:10.1103/PhysRevLett.120.171802`, `arXiv:1708.08856`.

[14] LHCb Collaboration, "Test of Lepton Flavor Universality by the measurement of the $B^0 \to D^{*-}\tau^+\nu_\tau$ branching fraction using three-prong τ decays", *Phys. Rev. D* **97** (2018), no. 7, 072013, `doi:10.1103/PhysRevD.97.072013`, `arXiv:1711.02505`.

[15] B. Dumont, K. Nishiwaki, and R. Watanabe, "LHC constraints and prospects for S_1 scalar leptoquark explaining the $\bar{B} \to D^{(*)}\tau\bar{\nu}$ anomaly", *Phys. Rev. D* **94** (2016) 034001, `doi:10.1103/PhysRevD.94.034001`, `arXiv:1603.05248`.

[16] H. Georgi and S. L. Glashow, "Unity of all elementary particle forces", *Phys. Rev. Lett.* **32** (1974) 438, `doi:10.1103/PhysRevLett.32.438`.

[17] J. C. Pati and A. Salam, "Unified lepton-hadron symmetry and a gauge theory of the basic interactions", *Phys. Rev. D* **8** (1973) 1240, `doi:10.1103/PhysRevD.8.1240`.

[18] J. C. Pati and A. Salam, "Lepton number as the fourth color", *Phys. Rev. D* **10** (1974) 275, `doi:10.1103/PhysRevD.10.275`. [Erratum: `doi:10.1103/PhysRevD.11.703.2`].

[19] H. Murayama and T. Yanagida, "A viable SU(5) GUT with light leptoquark bosons", *Mod. Phys. Lett. A* **7** (1992) 147, `doi:10.1142/S0217732392000070`.

[20] H. Fritzsch and P. Minkowski, "Unified interactions of leptons and hadrons", *Annals Phys.* **93** (1975) 193, `doi:10.1016/0003-4916(75)90211-0`.

[21] G. Senjanovic and A. Sokorac, "Light leptoquarks in SO(10)", *Z. Phys. C* **20** (1983) 255, `doi:10.1007/BF01574858`.

[22] P. H. Frampton and B.-H. Lee, "SU(15) grand unification", *Phys. Rev. Lett.* **64** (1990) 619, `doi:10.1103/PhysRevLett.64.619`.

[23] P. H. Frampton and T. W. Kephart, "Higgs sector and proton decay in SU(15) grand unification", *Phys. Rev. D* **42** (1990) 3892, `doi:10.1103/PhysRevD.42.3892`.

[24] S. Dimopoulos and L. Susskind, "Mass without scalars", *Nucl. Phys. B* **155** (1979) 237, `doi:10.1016/0550-3213(79)90364-X`.

[25] S. Dimopoulos, "Technicolored signatures", *Nucl. Phys. B* **168** (1980) 69, `doi:10.1016/0550-3213(80)90277-1`.

[26] E. Farhi and L. Susskind, "Technicolor", *Phys. Rept.* **74** (1981) 277, `doi:10.1016/0370-1573(81)90173-3`.

[27] B. Schrempp and F. Schrempp, "Light leptoquarks", *Phys. Lett. B* **153** (1985) 101, `doi:10.1016/0370-2693(85)91450-9`.

[28] M. Tanaka and R. Watanabe, "New physics in the weak interaction of $\bar{B} \to D^{(*)}\tau\bar{\nu}$", *Phys. Rev. D* **87** (2013) 034028, `doi:10.1103/PhysRevD.87.034028`, `arXiv:1212.1878`.

[29] Y. Sakaki, M. Tanaka, A. Tayduganov, and R. Watanabe, "Testing leptoquark models in $\bar{B} \to D^{(*)}\tau\bar{\nu}$", *Phys. Rev. D* **88** (2013) 094012, `doi:10.1103/PhysRevD.88.094012`, `arXiv:1309.0301`.

[30] I. Doršner, S. Fajfer, N. Košnik, and I. Nišandžić, "Minimally flavored colored scalar in $\bar{B} \to D^{(*)}\tau\bar{\nu}$ and the mass matrices constraints", *JHEP* **11** (2013) 084, `doi:10.1007/JHEP11(2013)084`, `arXiv:1306.6493`.

[31] B. Gripaios, M. Nardecchia, and S. A. Renner, "Composite leptoquarks and anomalies in b-meson decays", *JHEP* **05** (2015) 006, `doi:10.1007/JHEP05(2015)006`, `arXiv:1412.1791`.

[32] M. Bauer and M. Neubert, "Minimal leptoquark explanation for the $R_{D^{(*)}}$, R_K , and $(g-2)_\mu$ anomalies", *Phys. Rev. Lett.* **116** (2016) 141802, `doi:10.1103/PhysRevLett.116.141802`, `arXiv:1511.01900`.

[33] R. Barbieri, G. Isidori, A. Pattori, and F. Senia, "Anomalies in B-decays and $U(2)$ flavour symmetry", *Eur. Phys. J. C* **76** (2016), no. 2, 67, `doi:10.1140/epjc/s10052-016-3905-3`, `arXiv:1512.01560`.

[34] I. Doršner et al., "Physics of leptoquarks in precision experiments and at particle colliders", *Phys. Rept.* **641** (2016) 1, `doi:10.1016/j.physrep.2016.06.001`, `arXiv:1603.04993`.

[35] D. Bečirević and O. Sumensari, "A leptoquark model to accommodate $R_K^{\mathrm{exp}} < R_K^{\mathrm{SM}}$ and $R_{K^*}^{\mathrm{exp}} < R_{K^*}^{\mathrm{SM}}$", *JHEP* **08** (2017) 104, `doi:10.1007/JHEP08(2017)104`, `arXiv:1704.05835`.

[36] D. Buttazzo, A. Greljo, G. Isidori, and D. Marzocca, "B-physics anomalies: a guide to combined explanations", *JHEP* **11** (2017) 044, `doi:10.1007/JHEP11(2017)044`, `arXiv:1706.07808`.

[37] E. Coluccio Leskow, G. DAmbrosio, A. Crivellin, and D. Muller, "$(g-2)_\mu$, lepton flavor violation, and Z decays with leptoquarks: Correlations and future prospects", *Phys. Rev. D* **95** (2017) 055018, `doi:10.1103/PhysRevD.95.055018`, `arXiv:1612.06858`.

[38] A. Crivellin, D. Müller, and T. Ota, "Simultaneous explanation of $R(D^{(*)})$ and $b \to s\mu^+\mu^-$: the last scalar leptoquarks standing", *JHEP* **09** (2017) 040, `doi:10.1007/JHEP09(2017)040`, `arXiv:1703.09226`.

[39] G. Hiller and I. Nišandžić, "R_K and R_{K^*} beyond the standard model", *Phys. Rev. D* **96** (2017) 035003, `doi:10.1103/PhysRevD.96.035003`, `arXiv:1704.05444`.

[40] I. Doršner, S. Fajfer, D. A. Faroughy, and N. Košnik, "The role of the S_3 GUT leptoquark in flavor universality and collider searches", *JHEP* **10** (2017) 188, `doi:10.1007/JHEP10(2017)188`, `arXiv:1706.07779`.

[41] L. Di Luzio, A. Greljo, and M. Nardecchia, "Gauge leptoquark as the origin of B-physics anomalies", *Phys. Rev. D* **96** (2017), no. 11, 115011, `doi:10.1103/PhysRevD.96.115011`, `arXiv:1708.08450`.

[42] L. Calibbi, A. Crivellin, and T. Li, "Model of vector leptoquarks in view of the B-physics anomalies", *Phys. Rev. D* **98** (2018), no. 11, 115002, `doi:10.1103/PhysRevD.98.115002`, `arXiv:1709.00692`.

[43] M. Bordone, C. Cornella, J. Fuentes-Martín, and G. Isidori, "A three-site gauge model for flavor hierarchies and flavor anomalies", *Phys. Lett. B* **779** (2018) 317, `doi:10.1016/j.physletb.2018.02.011`, `arXiv:1712.01368`.

[44] G. Hiller, D. Loose, and I. Nišandžić, "Flavorful leptoquarks at hadron colliders", *Phys. Rev. D* **97** (2018) 075004, `doi:10.1103/PhysRevD.97.075004`, `arXiv:1801.09399`.

[45] D. Bečirević et al., "Scalar leptoquarks from grand unified theories to accommodate the *B*-physics anomalies", *Phys. Rev. D* **98** (2018), no. 5, 055003, `doi:10.1103/PhysRevD.98.055003`, `arXiv:1806.05689`.

[46] L. Di Luzio et al., "Maximal Flavour Violation: a Cabibbo mechanism for leptoquarks", *JHEP* **11** (2018) 081, `doi:10.1007/JHEP11(2018)081`, `arXiv:1808.00942`.

[47] R. Barbieri and A. Tesi, "*B*-decay anomalies in Pati-Salam SU(4)", *Eur. Phys. J. C* **78** (2018), no. 3, 193, `doi:10.1140/epjc/s10052-018-5680-9`, `arXiv:1712.06844`.

[48] D. Marzocca, "Addressing the B-physics anomalies in a fundamental Composite Higgs Model", *JHEP* **07** (2018) 121, `doi:10.1007/JHEP07(2018)121`, `arXiv:1803.10972`.

[49] A. Angelescu, D. Becirevic, D. A. Faroughy, and O. Sumensari, "Closing the window on single leptoquark solutions to the *B*-physics anomalies", *JHEP* **10** (2018) 183, `doi:10.1007/JHEP10(2018)183`, `arXiv:1808.08179`.

[50] M. J. Baker, J. Fuentes-Martín, G. Isidori, and M. König, "High-p_T signatures in vector–leptoquark models", *Eur. Phys. J. C* **79** (2019), no. 4, 334, `doi:10.1140/epjc/s10052-019-6853-x`, `arXiv:1901.10480`.

[51] C. Cornella, J. Fuentes-Martín, and G. Isidori, "Revisiting the vector leptoquark explanation of the B-physics anomalies", *JHEP* **07** (2019) 168, `doi:10.1007/JHEP07(2019)168`, `arXiv:1903.11517`.

[52] C. Cornella et al., "Reading the footprints of the B-meson flavor anomalies", *JHEP* **08** (2021) 050, `doi:10.1007/JHEP08(2021)050`, `arXiv:2103.16558`.

[53] G. Isidori, D. Lancierini, P. Owen, and N. Serra, "On the significance of new physics in $b \to s\ell^+\ell^-$ decays", *Phys. Lett. B* **822** (2021) 136644, `doi:10.1016/j.physletb.2021.136644`, `arXiv:2104.05631`.

[54] LHCb Collaboration, "Differential branching fractions and isospin asymmetries of $B \to K^{(*)}\mu^+\mu^-$ decays", *JHEP* **06** (2014) 133, `doi:10.1007/JHEP06(2014)133`, `arXiv:1403.8044`.

[55] LHCb Collaboration, "Measurements of the S-wave fraction in $B^0 \to K^+\pi^-\mu^+\mu^-$ decays and the $B^0 \to K^*(892)^0\mu^+\mu^-$ differential branching fraction", *JHEP* **11** (2016) 047, `doi:10.1007/JHEP11(2016)047`, `arXiv:1606.04731`. [Erratum: `doi:10.1007/JHEP04(2017)142`].

[56] LHCb Collaboration, "Angular analysis and differential branching fraction of the decay $B_s^0 \to \phi\mu^+\mu^-$", *JHEP* **09** (2015) 179, `doi:10.1007/JHEP09(2015)179`, `arXiv:1506.08777`.

[57] LHCb Collaboration, "Angular analysis of the $B^0 \to K^{*0}\mu^+\mu^-$ decay using 3 fb^{-1} of integrated luminosity", *JHEP* **02** (2016) 104, `doi:10.1007/JHEP02(2016)104`, `arXiv:1512.04442`.

[58] LHCb Collaboration, "Test of lepton universality using $B^+ \to K^+\ell^+\ell^-$ decays", *Phys. Rev. Lett.* **113** (2014) 151601, `doi:10.1103/PhysRevLett.113.151601`, `arXiv:1406.6482`.

[59] LHCb Collaboration, "Test of lepton universality with $B^0 \to K^{*0}\ell^+\ell^-$ decays", *JHEP* **08** (2017) 055, `doi:10.1007/JHEP08(2017)055`, `arXiv:1705.05802`.

[60] LHCb Collaboration, "Search for lepton-universality violation in $B^+ \to K^+\ell^+\ell^-$ decays", *Phys. Rev. Lett.* **122** (2019), no. 19, 191801, `doi:10.1103/PhysRevLett.122.191801`, `arXiv:1903.09252`.

[61] LHCb Collaboration, "Test of lepton universality in beauty-quark decays", *Nature Phys.* **18** (2022), no. 3, 277, `doi:10.1038/s41567-021-01478-8`, `arXiv:2103.11769`.

[62] LHCb Collaboration, "Tests of lepton universality using $B^0 \to K_S^0\ell^+\ell^-$ and $B^+ \to K^{*+}\ell^+\ell^-$ decays", *Phys. Rev. Lett.* **128** (2022), no. 19, 191802, `doi:10.1103/PhysRevLett.128.191802`, `arXiv:2110.09501`.

[63] Belle Collaboration, "Lepton-flavor-dependent angular analysis of $B \to K^*\ell^+\ell^-$", *Phys. Rev. Lett.* **118** (2017) 111801, `doi:10.1103/PhysRevLett.118.111801`, `arXiv:1612.05014`.

[64] I. Doršner and A. Greljo, "Leptoquark toolbox for precision collider studies", *JHEP* **05** (2018) 126, `doi:10.1007/JHEP05(2018)126`, `arXiv:1801.07641`.

[65] D. A. Faroughy, A. Greljo, and J. F. Kamenik, "Confronting lepton flavor universality violation in B decays with high-p_T tau lepton searches at LHC", *Phys. Lett. B* **764** (2017) 126, `doi:10.1016/j.physletb.2016.11.011`, `arXiv:1609.07138`.

[66] M. Schmaltz and Y.-M. Zhong, "The leptoquark Hunter's guide: large coupling", *JHEP* **01** (2019) 132, `doi:10.1007/JHEP01(2019)132`, `arXiv:1810.10017`.

[67] ATLAS Collaboration, "Search for new phenomena in pp collisions in final states with tau leptons, b-jets, and missing transverse momentum with the ATLAS detector", *Phys. Rev. D* **104** (2021), no. 11, 112005, `doi:10.1103/PhysRevD.104.112005`, `arXiv:2108.07665`.

[68] CMS Collaboration, "Search for a singly produced third-generation scalar leptoquark decaying to a τ lepton and a bottom quark in proton-proton collisions at $\sqrt{s} = 13$ TeV", *JHEP* **07** (2018) 115, `doi:10.1007/JHEP07(2018)115`, `arXiv:1806.03472`.

[69] CMS Collaboration, "Search for singly and pair-produced leptoquarks coupling to third-generation fermions in proton-proton collisions at $\sqrt{s} = 13$ TeV", *Phys. Lett. B* **819** (2021) 136446, `doi:10.1016/j.physletb.2021.136446`, `arXiv:2012.04178`.

[70] CMS Collaboration, "Searches for physics beyond the standard model with the M_{T2} variable in hadronic final states with and without disappearing tracks in proton-proton collisions at $\sqrt{s} = 13$ TeV", *Eur. Phys. J. C* **80** (2020), no. 1, 3, `doi:10.1140/epjc/s10052-019-7493-x`, `arXiv:1909.03460`.

[71] ATLAS Collaboration, "Search for pair production of third-generation scalar leptoquarks decaying into a top quark and a τ-lepton in pp collisions at $\sqrt{s} = 13$ TeV with the ATLAS detector", *JHEP* **06** (2021) 179, `doi:10.1007/JHEP06(2021)179`, `arXiv:2101.11582`.

[72] CMS Collaboration, "The CMS trigger system", *JINST* **12** (2017) P01020, `doi:10.1088/1748-0221/12/01/P01020`, `arXiv:1609.02366`.

[73] CMS Collaboration, "The CMS experiment at the CERN LHC", *JINST* **3** (2008) S08004, doi:10.1088/1748-0221/3/08/S08004, arXiv:1510.07488.

[74] J. Alwall et al., "The automated computation of tree-level and next-to-leading order differential cross sections, and their matching to parton shower simulations", *JHEP* **07** (2014) 079, doi:10.1007/JHEP07(2014)079, arXiv:1405.0301.

[75] J. Alwall et al., "Comparative study of various algorithms for the merging of parton showers and matrix elements in hadronic collisions", *Eur. Phys. J. C* **53** (2008) 473, doi:10.1140/epjc/s10052-007-0490-5, arXiv:0706.2569.

[76] R. Frederix and S. Frixione, "Merging meets matching in MC@NLO", *JHEP* **12** (2012) 061, doi:10.1007/JHEP12(2012)061, arXiv:1209.6215.

[77] P. Nason, "A new method for combining NLO QCD with shower Monte Carlo algorithms", *JHEP* **11** (2004) 040, doi:10.1088/1126-6708/2004/11/040, arXiv:hep-ph/0409146.

[78] S. Frixione, P. Nason, and C. Oleari, "Matching NLO QCD computations with parton shower simulations: the POWHEG method", *JHEP* **11** (2007) 070, doi:10.1088/1126-6708/2007/11/070, arXiv:0709.2092.

[79] S. Alioli, P. Nason, C. Oleari, and E. Re, "A general framework for implementing NLO calculations in shower Monte Carlo programs: the POWHEG BOX", *JHEP* **06** (2010) 043, doi:10.1007/JHEP06(2010)043, arXiv:1002.2581.

[80] S. Frixione, P. Nason, and G. Ridolfi, "A positive-weight next-to-leading-order Monte Carlo for heavy flavour hadroproduction", *JHEP* **09** (2007) 126, doi:10.1088/1126-6708/2007/09/126, arXiv:0707.3088.

[81] J. M. Campbell, R. K. Ellis, P. Nason, and E. Re, "Top-pair production and decay at NLO matched with parton showers", *JHEP* **04** (2015) 114, doi:10.1007/JHEP04(2015)114, arXiv:1412.1828.

[82] S. Alioli, P. Nason, C. Oleari, and E. Re, "NLO single-top production matched with shower in POWHEG: *s*- and *t*-channel contributions", *JHEP* **09** (2009) 111, doi:10.1088/1126-6708/2009/09/111, arXiv:0907.4076. [Erratum: doi:10.1007/JHEP02(2010)011].

[83] E. Re, "Single-top Wt-channel production matched with parton showers using the POWHEG method", *Eur. Phys. J. C* **71** (2011) 1547, doi:10.1140/epjc/s10052-011-1547-z, arXiv:1009.2450.

[84] Y. Li and F. Petriello, "Combining QCD and electroweak corrections to production in FEWZ", *Phys. Rev. D* **86** (2012) 094034, doi:10.1103/PhysRevD.86.094034, arXiv:1208.5967.

[85] M. Czakon and A. Mitov, "Top++: A program for the calculation of the top-pair cross-section at hadron colliders", *Comput. Phys. Commun.* **185** (2014) 2930, doi:10.1016/j.cpc.2014.06.021, arXiv:1112.5675.

[86] P. Kant et al., "HatHor for single top-quark production: Updated predictions and uncertainty estimates for single top-quark production in hadronic collisions", *Comput. Phys. Commun.* **191** (2015) 74, doi:10.1016/j.cpc.2015.02.001, arXiv:1406.4403.

[87] CMS Collaboration, "Event generator tunes obtained from underlying event and multiparton scattering measurements", *Eur. Phys. J. C* **76** (2016) 155, `doi:10.1140/epjc/s10052-016-3988-x`, `arXiv:1512.00815`.

[88] CMS Collaboration, "Extraction and validation of a new set of CMS PYTHIA8 tunes from underlying-event measurements", *Eur. Phys. J. C* **80** (2020) 4, `doi:10.1140/epjc/s10052-019-7499-4`, `arXiv:1903.12179`.

[89] CMS Collaboration, "Investigations of the impact of the parton shower tuning in Pythia 8 in the modelling of $t\bar{t}$ at $\sqrt{s} = 8$ and 13 TeV", CMS Physics Analysis Summary CMS-PAS-TOP-16-021, CERN, 2016.

[90] R. D. Ball et al., "Parton distributions for the LHC Run II", *JHEP* **15** (2015) 40, `doi:10.1007/JHEP04(2015)040`, `arXiv:1410.8849`.

[91] GEANT4 Collaboration, "GEANT4 — a simulation toolkit", *Nucl. Instrum. Meth. A* **506** (2003) 250, `doi:10.1016/S0168-9002(03)01368-8`.

[92] F. Maltoni and T. Stelzer, "Madevent: Automatic event generation with madgraph", *JHEP* **02** (2003) 027, `doi:10.1088/1126-6708/2003/02/027`, `arXiv:hep-ph/0208156`.

[93] T. Sjöstrand et al., "An introduction to PYTHIA 8.2", *Comput. Phys. Commun.* **191** (2015) 159, `doi:10.1016/j.cpc.2015.01.024`, `arXiv:1410.3012`.

[94] C. Borschensky, B. Fuks, A. Kulesza, and D. Schwartländer, "Scalar leptoquark pair production at hadron colliders", *Phys. Rev. D* **101** (2020), no. 11, 115017, `doi:10.1103/PhysRevD.101.115017`, `arXiv:2002.08971`.

[95] CMS Collaboration, "Particle-flow reconstruction and global event description with the CMS detector", *JINST* **12** (2017) P10003, `doi:10.1088/1748-0221/12/10/P10003`, `arXiv:1706.04965`.

[96] CMS Collaboration, "Technical proposal for the Phase-II upgrade of the Compact Muon Solenoid", CMS Technical Proposal CERN-LHCC-2015-010, CMS-TDR-15-02, CERN, 2015.

[97] H. Voss, A. Höcker, J. Stelzer, and F. Tegenfeldt, "TMVA, the toolkit for multivariate data analysis with ROOT", in *XI Int. Workshop on Advanced Computing and Analysis Techniques in Physics Research.* 2007. `arXiv:physics/0703039`. PoS ACAT:040.

[98] CMS Collaboration, "Performance of electron reconstruction and selection with the CMS detector in proton-proton collisions at $\sqrt{s} = 8$ TeV", *JINST* **10** (2015) P06005, `doi:10.1088/1748-0221/10/06/P06005`, `arXiv:1502.02701`.

[99] CMS Collaboration, "Performance of the CMS muon detector and muon reconstruction with proton-proton collisions at $\sqrt{s} = 13$ TeV", *JINST* **13** (2018) P06015, `doi:10.1088/1748-0221/13/06/P06015`, `arXiv:1804.04528`.

[100] M. Cacciari, G. P. Salam, and G. Soyez, "The anti-k_t jet clustering algorithm", *JHEP* **04** (2008) 063, `doi:10.1088/1126-6708/2008/04/063`, `arXiv:0802.1189`.

[101] M. Cacciari and G. P. Salam, "Dispelling the N^3 myth for the k_T jet-finder", *Phys. Lett. B* **641** (2006) 57, `doi:10.1016/j.physletb.2006.08.037`, `arXiv:hep-ph/0512210`.

[102] M. Cacciari, G. P. Salam, and G. Soyez, "FastJet user manual", *Eur. Phys. J. C* **72** (2012) 1896, `doi:10.1140/epjc/s10052-012-1896-2`, `arXiv:1111.6097`.

[103] CMS Collaboration, "Determination of jet energy calibration and transverse momentum resolution in CMS", *JINST* **6** (2011) P11002, `doi:10.1088/1748-0221/6/11/P11002`, `arXiv:1107.4277`.

[104] CMS Collaboration, "Pileup jet identification", CMS Physics Analysis Summary CMS-PAS-JME-13-005, CERN, 2013.

[105] CMS Collaboration, "Jet algorithms performance in 13 TeV data", CMS Physics Analysis Summary CMS-PAS-JME-16-003, CERN, 2017.

[106] D. Guest et al., "Jet Flavor Classification in High-Energy Physics with Deep Neural Networks", *Phys. Rev. D* **94** (2016), no. 11, 112002, `doi:10.1103/PhysRevD.94.112002`, `arXiv:1607.08633`.

[107] CMS Collaboration, "Identification of heavy-flavour jets with the CMS detector in pp collisions at 13 TeV", *JINST* **13** (2018), no. 05, P05011, `doi:10.1088/1748-0221/13/05/P05011`, `arXiv:1712.07158`.

[108] CMS Collaboration, "Performance of reconstruction and identification of τ leptons decaying to hadrons and ν_τ in pp collisions at $\sqrt{s} = 13$ TeV", *JINST* **13** (2018) P10005, `doi:10.1088/1748-0221/13/10/P10005`, `arXiv:1809.02816`.

[109] CMS Collaboration, "Identification of hadronic tau lepton decays using a deep neural network", *JINST* **17** (2022), no. 07, P07023, `doi:10.1088/1748-0221/17/07/p07023`, `arXiv:2201.08458`.

[110] CMS Collaboration, "Performance of missing energy reconstruction in 13 TeV pp collision data using the CMS detector", CMS Physics Analysis Summary CMS-PAS-JME-16-004, CERN, 2016.

[111] CMS Collaboration, "Performance of missing transverse momentum in pp collisions at $\sqrt{s} = 13$ TeV using the CMS detector", CMS Physics Analysis Summary CMS-PAS-JME-17-001, CERN, 2018.

[112] CMS Collaboration, "Search for additional neutral MSSM Higgs bosons in the $\tau\tau$ final state in proton-proton collisions at $\sqrt{s} = 13$ TeV", *JHEP* **09** (2018) 007, `doi:10.1007/JHEP09(2018)007`, `arXiv:1803.06553`.

[113] CMS Collaboration, "Measurement of the $Z\gamma^* \to \tau\tau$ cross section in pp collisions at $\sqrt{s} = 13$ TeV and validation of τ lepton analysis techniques", 2018. `arXiv:1801.03535`. Submitted to *EPJC*.

[114] CMS Collaboration, "Precision luminosity measurement in proton-proton collisions at $\sqrt{s} = 13$ TeV in 2015 and 2016 at CMS", *Eur. Phys. J. C* **81** (2021) 800, `doi:10.1140/epjc/s10052-021-09538-2`, `arXiv:2104.01927`.

[115] CMS Collaboration, "CMS luminosity measurement for the 2017 data-taking period at $\sqrt{s} = 13$ TeV", CMS Physics Analysis Summary CMS-PAS-LUM-17-004, CERN, 2018.

[116] CMS Collaboration, "CMS luminosity measurement for the 2018 data-taking period at $\sqrt{s} = 13$ TeV", CMS Physics Analysis Summary CMS-PAS-LUM-18-002, CERN, 2019.

[117] CMS Collaboration, "Observation of the Higgs boson decay to a pair of τ leptons with the CMS detector", *Phys. Lett. B* **779** (2018) 283, `doi:10.1016/j.physletb.2018.02.004,arXiv:1708.00373`.

[118] CMS Collaboration, "Performance of reconstruction and identification of tau leptons in their decays to hadrons and tau neutrino in LHC Run-2", CMS Physics Analysis Summary CMS-PAS-TAU-16-002, CERN, 2016.

[119] J. Butterworth et al., "PDF4LHC recommendations for LHC Run II", *J. Phys. G* **43** (2016) 023001, `doi:10.1088/0954-3899/43/2/023001,arXiv:1510.03865`.

[120] R. J. Barlow and C. Beeston, "Fitting using finite Monte Carlo samples", *Comput. Phys. Commun.* **77** (1993) 219, `doi:10.1016/0010-4655(93)90005-W`.

[121] J. S. Conway, "Incorporating Nuisance Parameters in Likelihoods for Multisource Spectra", in *PHYSTAT 2011*, p. 115. 2011. `arXiv:1103.0354`. `doi:10.5170/CERN-2011-006.115`.

[122] ATLAS and CMS Collaborations, "Procedure for the LHC Higgs boson search combination in summer 2011", Technical Report CMS-NOTE-2011-005, ATL-PHYS-PUB-2011-011, CERN, 2011.

[123] T. Junk, "Confidence level computation for combining searches with small statistics", *Nucl. Instrum. Meth. A* **434** (1999) 435, `doi:10.1016/S0168-9002(99)00498-2`, `arXiv:hep-ex/9902006`.

[124] A. L. Read, "Presentation of search results: The CL$_s$ technique", *J. Phys. G* **28** (2002) 2693, `doi:10.1088/0954-3899/28/10/313`.

[125] G. Cowan, K. Cranmer, E. Gross, and O. Vitells, "Asymptotic formulae for likelihood-based tests of new physics", *Eur. Phys. J. C* **71** (2011) `doi:10.1140/epjc/s10052-011-1554-0,arXiv:1007.1727`. [Erratum: `doi:10.1140/epjc/s10052-013-2501-z`].